Instabilities of a free bilayer flowing on an inclined porous medium

A. Ananth Praveen Kumar,[1] R. Usha,[2] Tamal Banerjee,[1] and Dipankar Bandyopadhyay[1,3,*]
[1]*Department of Chemical Engineering, Indian Institute of Technology Guwahati, India*
[2]*Department of Mathematics, Indian Institute of Technology, Chennai, India*
[3]*Centre for Nanotechnology, Indian Institute of Technology Guwahati, India*
(Received 27 July 2013; published 13 December 2013)

The instabilities of a free bilayer flowing on an inclined Darcy-Brinkman porous layer have been explored. The bilayer is composed of a pair of immiscible liquid films with a deformable liquid-liquid interface and a liquid-air free surface. An Orr-Sommerfeld analysis of the governing equations and boundary conditions uncovers that this configuration can be unstable by a pair of long-wave interfacial modes at the free surface and at the interface together with a couple of finite wave-number shear modes originating from the inertial influences at the liquid layers. In particular, one of the shear modes originates beyond a threshold flow rate owing to the slippage at the porous-liquid interface and is found to be the dominant one even when the porous medium is moderately thin, porous, and permeable. The strength of the porous media mediated mode (a) grows with increase in porosity, (b) grows and then remains invariant with increase in thickness, and (c) initially grows and then decays with increase in the permeability of the porous layer. Further, the presence of a lower layer with smaller viscosity and a thicker upper layer is found to facilitate the growth of this newly identified porous media mode. Importantly, beyond a threshold upper to lower thickness and viscosity ratios and the angle of inclination the porous media mode dominates over all the other interfacial or shear modes, highlighting its importance in the bilayer flows down an inclined porous medium. The study showcases the importance of a porous layer in destabilizing a free bilayer flow down an inclined plane, which can be of importance to improve mixing, emulsification, and heat and mass transfer characteristics in the microscale devices.

DOI: 10.1103/PhysRevE.88.063012 PACS number(s): 47.56.+r, 68.15.+e, 47.20.Ft, 47.61.Jd

I. INTRODUCTION

Stability and dynamics of multiple thin layers have gained attention for long owing to their appearance in diverse products and processes. At one end, instabilities in such configurations can improve the rate of mass, momentum, and heat transfer in the microscale devices while in the other end, the interfacial stability is essential to increase the life span of protective coatings or photographic films. The oil-water flow, polymer extrusion [1–3], electrochemical and fuel cells [4,5], microfluidic devices [6,7], and bioprocesses [8] are also some common examples where the interfacial instability and subsequent dynamics of the multilayer films play an important role in ensuring mechanical, electrical, thermal, optical, and barrier properties of the finished products. The studies related to the instabilities of the multiphase systems also uncover many interesting aspects of fundamental science which include the origin of the squeezing (varicose) or bending (sinuous) modes at the interfaces, pattern formation, phase separation of immiscible layers, formation of embedded and encapsulated structures, coalescence or pinching-off of the droplets, and contact line motion, among many others. The salient features of the stability and dynamics of various multilayer configurations in the macro-, micro-, and nanoscale regimes are ably summarized in a host of review articles [9–15].

Among the multilayer configurations, the two-layer flows can largely be classified into (i) confined bilayer—a pair of immiscible films is confined between a pair of bounding substrates with a common deformable interface, and (ii) free bilayer—a pair of immiscible films with a free surface and an interface resting or flowing on a substrate (Fig. 1). The macroscopic behaviors of the confined bilayer is explored by a number of previous works, both theoretically [16–33] and experimentally [34,35]. Yih [16] reported the presence of the long-wave interfacial mode of instability in the confined two-layer plane Poiseuille (PPF) and Couette (CF) flows originating from the viscosity stratification of the liquid layers across the deformable interface. Later, Hooper and Boyd [17] found the Tollmein-Schlichting type finite-wave-number shear mode of instability beyond a threshold flow rate in a confined bilayer undergoing CF. At lower flow rates, Yiantsios and Higgins [18] and Hooper [17] summarized that a confined bilayer undergoing PPF could either be neutrally stable when $\mu_r = h_r^2$ or could be unstable by the interfacial (shear) mode of instability when the condition $\mu_r > h_r^2$ ($\mu_r < h_r^2$) is met. Here $\mu_r$and $h_r$denote viscosity and the thickness ratios of the liquid layers, respectively. Subsequent studies showed that in the nonlinear regime, a linearly unstable interface could evolve into the undisturbed state or to a finite amplitude steady state [19]. The thin-layer effect with a more viscous layer is confined between a semi-infinite layer and a solid wall had also been studied in detail over the years [20,27–31]. In addition, a number of studies reported the presence of the multiple (odd or even) finite wave-number shear modes for a confined bilayer including the effects of the inclination of the substrate [32,33].

Similar to the confined bilayer, the interfacial instabilities of the macroscopic free bilayers have also been studied extensively. The instabilities in the free bilayers are rather different from those in the confined bilayers because of the presence of the coupled deformable liquid-air surface and liquid-liquid interface. Kao [36–38] identified surface and

*Author to whom correspondence should be addressed: dipban@iitg.ernet.in

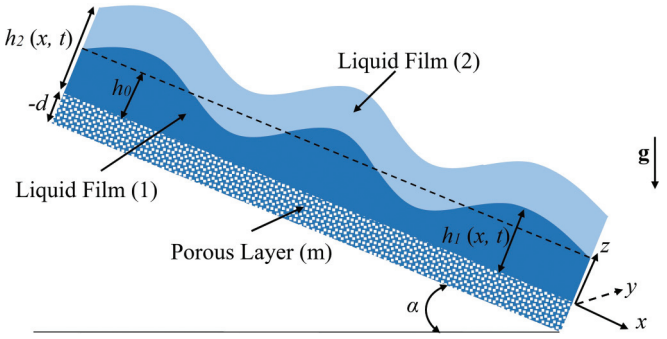

FIG. 1. (Color online) Schematic diagram of the flow of a free bilayer on an inclined porous medium.

interfacial modes of instabilities while considering the effects of both viscosity and density stratifications. Later, it was found that much like the confined bilayers, the interfacial mode of instability was more apparent when the upper layer viscosity is higher [39–41]. The traveling interfacial modes under varied conditions were also simulated employing long-wave nonlinear simulations to uncover the role of the interfacial shear on the evolution of the instability [42–44]. Attempts were also made to predict the wave velocity and growth rate of the interfacial modes employing a longitudinal velocity perturbation associated with the surface and interfacial deflections [45]. Further, a lot of attention has been paid to uncover the convective nature of the unstable modes [46] and to identify the importance of the flexibility of the underlying substrate [47]. Importantly, the studies reported that other than the viscosity and density stratification, the interfacial modes of instabilities of a free bilayer down an inclined plane could be under various stabilizing or destabilizing inertial influences depending on the position of the more or less viscous liquid film [47]. For example, when the less viscous fluid is adjacent to the inclined wall, inertia can stabilize the interfacial mode at the liquid-liquid interface whereas the same effect can destabilize the liquid-air free surface. In contrast, inertia destabilizes both the interfacial modes when the more viscous layer is adjacent to the inclined wall.

Apart from the studies related to the macroscopic confined and free bilayers, a number of recent works explore the potential of these configurations in the micro or nanoscale pattern formation [48,49], pumping [50], and mixing or demixing [51–58]. Especially, it is now a well-established fact that at smaller dimensions, even a little defect, roughness, porosity, and slippage at the bounding surfaces can notably alter the flow dynamics. However, the behaviors of liquid layers adjacent to the porous layers are quite complex and interesting. For example, Beavers and Joseph [59] showed the influence of a porous layer on a macroscopic flow with the help of a semiempirical slip boundary condition at the porous-liquid interface. Later, employing a more comprehensive Darcy's law for the porous medium the destabilizing effect of permeability was identified for a flow over an inclined porous plane [60–66]. Some of the more recent works show that the use of a generic Darcy-Brinkman transport equation for the porous layer can unveil finer details on the influence of the different properties of porous layers such as the porosity, permeability, and stress jump coefficient on the instabilities of thin films on a porous substrate [67–80]. In particular, it was identified that the presence of a porous medium can indeed change the force distribution in the layers to engender additional modes of instabilities especially when the film thickness is smaller and the flow is laminar [81,82]. Importantly, the studies uncover that for a confined bilayer, the interlayer mixing can be enhanced only by tuning the porous media parameters such as the thickness, the porosity, and the permeability of the porous layer.

However, most of the previous studies consider either a single layer or a confined bilayer while discussing the influence of the porous medium. The hydrodynamic instabilities of a free bilayer on an inclined porous medium (Fig. 1) is another interesting configuration to be explored in detail. In the present work, with the help of an Orr-Sommerfeld (OS) analysis of the governing equations and boundary conditions, the instabilities of a free bilayer on an inclined porous medium described by Darcy-Brinkman model have been studied. Previous studies indicate that a free bilayer can be unstable by surface modes at the liquid-air free surface and interfacial modes at the liquid-liquid interface. In this work, we highlight the influences of the porous layer properties on these two modes. We also identify additional modes of instabilities that can originate from the underlying porous layer. In order to ensure the accuracy of the results, the OS system is solved employing two different numerical techniques. An eigenfunction analysis is also performed to identify the critical layers and the location of the finite wave-number modes of the instabilities. Interestingly, the analysis uncovers that, for a fixed Reynolds number, thickness, and viscosity ratio, the porous medium parameters can stimulate an entirely new finite wave-number shear mode of instability while the instability modes remain dormant to these influences. The results discussed here can be of importance in improving the microscale mixing, heat and mass transfer, emulsification, and phase separation of free bilayer flows.

The paper is organized in the following manner: Section II shows the problem formulation in which the governing equations and boundary conditions are discussed. The base state velocity profiles are discussed in Sec. III. In Secs. IV and V, the linear stability analysis and the numerical methods to solve the OS system are discussed. The results are analyzed in Sec. VI followed by the conclusions in Sec. VII.

II. PROBLEM FORMULATION

Figure 1 schematically shows the free bilayer configuration considered in this work. In the formulation, the origin is fixed at the porous-liquid interface ($z = 0$) and the unit vectors ($\mathbf{e_x}$, $\mathbf{e_z}$) for the two-dimensional (2D) flow are directed along the x and z directions. The variables for the lower (upper) liquid layers are denoted by the subscripts 1 (2) and the variable for the porous medium can be identified from the subscript m. The films are assumed to be Newtonian, isothermal, incompressible, and immiscible. The films are also considered to possess constant density (ρ_j) and viscosity (μ_j). The bilayer flows over a Darcy-Brinkman porous medium of porosity δ, permeability κ, and thickness d. The continuity and the equations of motions for the films ($j = 1$ and 2) in the vector

form are

$$\nabla \cdot \mathbf{u}_j = 0, \tag{2.1}$$

$$\rho_j[\dot{\mathbf{u}}_j + (\mathbf{u}_j \cdot \nabla)\mathbf{u}_j] = -\nabla p_j + \mu_j \nabla^2 \mathbf{u}_j + \rho_j \mathbf{g}. \tag{2.2}$$

The mass and momentum balance for the Darcy-Brinkman porous medium [67–70] are

$$\nabla \cdot \mathbf{u}_m = 0, \tag{2.3}$$

$$\frac{\rho_1}{\delta}\dot{\mathbf{u}}_m = -\nabla p_m + \mu_e \nabla^2 \mathbf{u}_m - \frac{\mu_1}{\kappa}\mathbf{u}_m + \rho_1 \mathbf{g}. \tag{2.4}$$

In Eqs. (2.1)–(2.4), the notations, $\mathbf{g}$, $\mathbf{u}_j\{u_j, w_j\}$, and p_j represent the acceleration due to gravity, the velocity vector, and the pressure for the layers $j = 1, 2$, and m, respectively. The overdots represent the time derivative and the porosity is defined as the ratio of the lower layer viscosity to the effective viscosity of the porous layer ($\delta = \mu_1/\mu_e$). No-slip and no-penetration conditions are applied as boundary conditions at the porous-solid interface ($z = -d$),

$$\mathbf{u}_m = 0. \tag{2.5}$$

The continuity of normal stress, jump in the tangential stress, and continuity of the velocities are enforced as boundary conditions at the porous-liquid interface ($z = 0$),

$$\mathbf{u}_1 = \mathbf{u}_m, \tag{2.6}$$

$$-p_m + 2\mu_e w_{mz} = -p_1 + 2\mu_1 w_{1z}, \tag{2.7}$$

$$\mu_e u_{mz} - \mu_1 u_{1z} = \frac{\xi}{\sqrt{\kappa}} u_m. \tag{2.8}$$

Here, the jump coefficient ξ is the measure of spatial heterogeneity at the porous-liquid interface [68] and the subscripts x and z denote partial derivatives. The normal and tangential stress balances and the continuity of the velocities are enforced as boundary conditions at the liquid-liquid interface ($z = h_1$),

$$\mathbf{n}_1 \cdot \bar{\boldsymbol{\tau}}_2 \cdot \mathbf{n}_1 - \mathbf{n}_1 \cdot \bar{\boldsymbol{\tau}}_1 \cdot \mathbf{n}_1 = \gamma_1(\nabla \cdot \mathbf{n}_1), \tag{2.9}$$

$$\mathbf{t}_1 \cdot \bar{\boldsymbol{\tau}}_2 \cdot \mathbf{n}_1 = \mathbf{t}_1 \cdot \bar{\boldsymbol{\tau}}_1 \cdot \mathbf{n}_1, \tag{2.10}$$

$$\mathbf{u}_1 = \mathbf{u}_2. \tag{2.11}$$

Here h_1 represents the thickness of the lower layer, γ_1 represents the interfacial tension of the liquid-liquid interface, $\bar{\boldsymbol{\tau}}_j$ is the stress tensor, ∇ is gradient operator, $\mathbf{n}_i\,[(-h_{ix}/\sqrt{(1+h_{ix}^2)}, 1/\sqrt{(1+h_{ix}^2)})]$ and $\mathbf{t}_i\,[(1/\sqrt{(1+h_{ix}^2)}, h_{ix}/\sqrt{(1+h_{ix}^2)})]$ are the outward normal and tangent vectors, respectively. The location of the liquid-liquid interface ($y = h_1$) is defined by the kinematic condition

$$\dot{h}_1 = -u_1(\partial h_1/\partial x) + w_1. \tag{2.12}$$

At free surface ($z = h_2$), the normal and tangential stress balances and the kinematic condition are enforced as boundary conditions,

$$\mathbf{n}_2 \cdot \bar{\boldsymbol{\tau}}_2 \cdot \mathbf{n}_2 = \gamma_2(\nabla \cdot \mathbf{n}_2), \tag{2.13}$$

$$\mathbf{t}_2 \cdot \bar{\boldsymbol{\tau}}_2 \cdot \mathbf{n}_2 = 0, \tag{2.14}$$

$$\dot{h}_2 = -u_2(\partial h_2/\partial x) + w_2. \tag{2.15}$$

Here h_2 represents the combined thickness of the liquid layers and γ_2 represents the surface tension of the liquid-air interface.

Equations (2.1)–(2.15) are transformed into nondimensional forms employing the base state lower layer thickness (h_0) as length scale and $\rho_1 h_0^2/\mu_1$ as the time scale. The resulting set of dimensionless variables is $X = x/h_0$, $Z = z/h_0$, $D_m = d/h_0$, $H_1 = h_1/h_0$, $H_2 = h_2/h_0$, $T = t\mu_1/\rho_1 h_0^2$, $\mathbf{U}_j = \mathbf{u}_j \rho_1 h_0/\mu_1$, $\rho_r = \rho_2/\rho_1$, $\mu_r = \mu_2/\mu_1$, $h_r = (h_2/h_1) - 1$, $G = g h_0^3/\nu_1^2$, $\Gamma_1 = \gamma_1 h_0/\rho_1 \nu_1^2$, $\Gamma_2 = \gamma_2 h_0/\rho_1 \nu_1^2$, and $P_j = p_j h_0^2 \rho_1/\mu_1^2$. In the following equations, the subscripts X and Z denote partial derivatives. At the base state, the lower, upper, and porous layers occupy $0 \leqslant Z \leqslant H_1$, $H_1 \leqslant Z \leqslant H_2$, and $-D_m \leqslant Z \leqslant 0$, where H_1 is the position of the liquid-liquid interface and H_2 represents the location of the liquid-air interface. The dimensionless continuity equations for the films and the porous layer are as follows:

$$U_{1X} + W_{1Z} = 0, \tag{2.16}$$

$$U_{2X} + W_{2Z} = 0, \tag{2.17}$$

$$U_{mX} + W_{mZ} = 0. \tag{2.18}$$

The X and Z components of the dimensionless momentum equations for the liquid and porous layers are

$$\dot{U}_1 + U_1 U_{1X} + W_1 U_{1Z} = -P_{1X} + (U_{1XX} + U_{1ZZ}) + G\sin\alpha, \tag{2.19}$$

$$\dot{W}_1 + U_1 W_{1X} + W_1 W_{1Z} = -P_{1Z} + (W_{1XX} + W_{1ZZ}) - G\cos\alpha, \tag{2.20}$$

$$\rho_r(\dot{U}_2 + U_2 U_{2X} + W_2 U_{2Z}) = -P_{2X} + \mu_r(U_{2XX} + U_{2ZZ}) + \rho_r G\sin\alpha. \tag{2.21}$$

$$\rho_r(\dot{W}_2 + U_2 W_{2X} + W_2 W_{2Z}) = -P_{2Z} + \mu_r(W_{2XX} + W_{2ZZ}) - \rho_r G\cos\alpha, \tag{2.22}$$

$$(1/\delta)\dot{U}_m = -P_{mX} + (1/\delta)(U_{mXX} + U_{mZZ}) - (1/\mathrm{Da})U_m + G\sin\alpha, \tag{2.23}$$

$$(1/\delta)\dot{W}_m = -P_{mZ} + (1/\delta)(W_{mXX} + W_{mZZ}) - (1/\mathrm{Da})W_m - G\cos\alpha. \tag{2.24}$$

The no-slip and no-penetration boundary conditions at the porous-solid interface ($Z = -D_m$),

$$U_m = W_m = 0. \tag{2.25}$$

The continuity of X and Z components of velocities, the stress jump condition, and the normal stress balance at the porous-liquid interface ($Z = 0$) are

$$U_1 = U_m, \tag{2.26}$$

$$W_1 = W_m, \tag{2.27}$$

$$(1/\delta)U_{mZ} - U_{1Z} - (\chi/\sqrt{\mathrm{Da}})U_m = 0, \tag{2.28}$$

$$P_1 - P_m + 2[(1/\delta)W_{mZ} - W_{1Z}] = 0. \tag{2.29}$$

The continuity of velocities, normal and tangential stress balances, and the kinematic condition at the liquid-liquid interface ($Z = H_1$) are

$$U_1 = U_2, \tag{2.30}$$

$$W_1 = W_2, \tag{2.31}$$

$$P_2 - P_1 + \frac{2}{\left[1 + H_{1X}^2\right]}\left\{\left[\left(1 - H_{1X}^2\right) W_{1Z} - H_{1X}(W_{1X} + U_{1Z})\right]\right\} - \mu_r\left[\left(1 - H_{1X}^2\right) W_{2Z} - H_{1X}(W_{2X} + U_{2Z})\right] = \frac{\Gamma H_{1XX}}{\left[1 + H_{1X}^2\right]^{3/2}}, \tag{2.32}$$

$$\left[(U_{1Z} + W_{1X})\left(1 - H_{1X}^2\right) + 2H_{1X}\left(W_{1Z} - U_{1X}\right)\right] - \mu_r\left[(U_{2Z} + W_{2X})\left(1 - H_{1X}^2\right) + 2H_{1X}\left(W_{2Z} - U_{2X}\right)\right] = 0, \tag{2.33}$$

$$\dot{H}_1 = -U_1 H_{1X} + W_1. \tag{2.34}$$

The normal and tangential stress balances and the kinematic condition at the liquid-air interface ($Z = H_2$) are

$$-P_2 + \frac{2\mu_r}{\left[1 + H_{2X}^2\right]}\left(\left\{\left[\left(1 - H_{2X}^2\right) W_{2Z} - H_{2X}(W_{2X} + U_{2Z})\right]\right\}\right) = \frac{\Gamma_2 H_{XX}}{\left[1 + H_{2X}^2\right]^{3/2}}, \tag{2.35}$$

$$\left[(U_{2Z} + W_{2X})\left(1 - H_X^2\right) + 2H_X(W_{2Z} - U_{2X})\right] = 0, \tag{2.36}$$

$$\dot{H}_2 = -U_2 H_{2X} + W_2. \tag{2.37}$$

In Eqs. (2.16)–(2.37), the parameters $\mathrm{Da} = \kappa/h_0^2$, $\chi = \xi/\mu_1$, G, and $\Gamma_j = \gamma_j h_0/\rho_1 v_1^2$ denote the Darcy number, dimensionless stress jump coefficient, and Galileo and Capillary numbers, respectively. In what follows, the discussions are carried out in terms of the nondimensional variables.

III. BASE STATE

The governing equations and the boundary conditions are simplified with the following variables for the unperturbed interfaces to obtain the base state solutions of the x-directional flow:

$$\begin{aligned} &H_1 = 1, \quad H_2 = \bar{H}_2, \quad \bar{W}_j = 0, \quad \text{and} \\ &U_j = \bar{U}_j(Z)\ (j = 1,2, \text{ and } m). \end{aligned} \tag{3.1}$$

The overbars indicate base-state variables. The expressions for the velocity profiles for the base state are

$$\bar{U}_1 = C_{11}Z^2 + C_{12}Z + C_{13}, \quad 0 \leqslant Z \leqslant 1, \tag{3.2}$$

$$\bar{U}_2 = C_{21}Z^2 + C_{22}Z + C_{23}, \quad 1 \leqslant Z \leqslant H_2, \tag{3.3}$$

$$\bar{U}_m = C_{m1}e^{MZ} + C_{m2}e^{-MZ} + C_{m3}, \quad -D_m \leqslant Z \leqslant 0. \tag{3.4}$$

Here $\bar{U}_1$, $\bar{U}_2$, and $\bar{U}_m$ represent the base state velocities at the lower, upper, and porous layers, respectively, and $M = \sqrt{\delta/\mathrm{Da}}$. A brief derivation of the base state equations and the expressions for the constants C_{ij} ($i = 1$, 2, and m; $j = 1$, 2, and 3) in Eqs. (3.2)–(3.4) are shown in the Appendix.

Figure 2 summarizes the base state velocity profiles under various conditions. Plot (a) shows, with an increase in porosity (δ), that the flow in the porous layer becomes stronger, which in turn induces a larger slippage at the porous-liquid interface. The velocities in the liquid layer increase with an increase in δ. Plot (b) shows that an increase in the thickness of the porous layer can also impart larger slippage to the porous-liquid interface until a limiting value of the porous layer thickness. The curves in this plot suggest that the flow in the liquid layers is influenced by the increase in the porous layer thickness only in the regime where D_m is less than 1.0. Permeability in the porous layer is another parameter that can enhance the inertial influence to the liquid layers, as shown by plot (c). The curves in this figure suggest that the flow inside the porous layer becomes stronger with an increase in Da. Plots (a)–(c) clearly indicate that the free bilayers flowing over a porous medium can experience an enhanced inertial influence owing to the flow inside the porous layer, which can significantly alter the stability characteristics. Plots (d) and (e) show that the flow is stronger in the porous layer when the less viscous fluid is adjacent to the porous layer. Also, the flow rate is more when the lower liquid layer close to the porous layer has less density and less viscosity than the upper fluid layer [plot (e)]. It may be noted here that for free bilayers, the location of maximum velocity is always at the liquid-air interface, even when the bilayer is composed of a denser or a more viscous

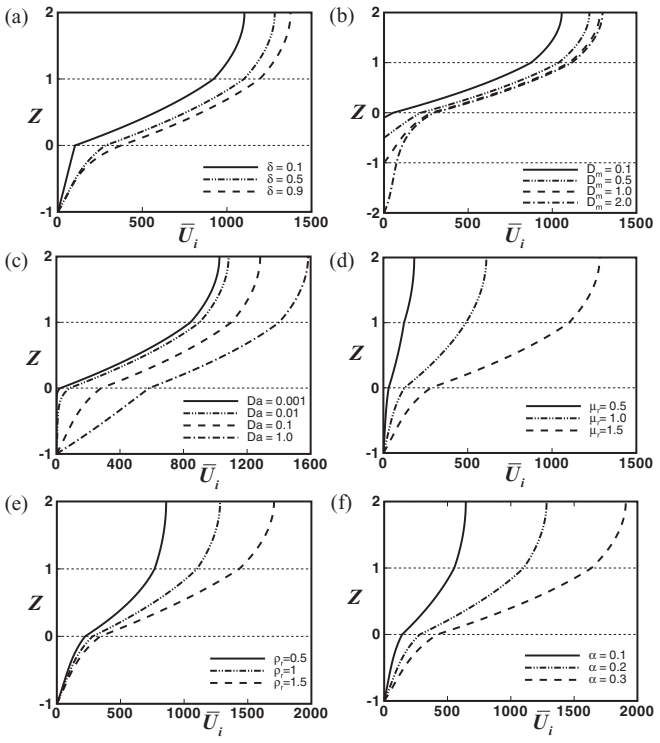

FIG. 2. Plots show the nondimensional base state velocity ($\bar{U}_i$) profiles across the width of the channel (Z) when $h_r = 1$. The curves in plots (a)–(f) correspond to different δ, D_m, Da, μ_r, ρ_r, and α respectively. The other parameters are fixed at $\delta = 0.5$, $D_m = 1$, Da $= 0.1$,$\rho_r = 1$,$\mu_r = 1.5$, $\Gamma_1 = 8 \times 10^3$, $\Gamma_2 = 15 \times 10^3$, and $\alpha = 0.2$.

upper layer (solid lines). Plot (f) shows that an increase in the angle of inclination can intensify the flow inside both the porous and liquid layers. Plots (d)–(f) summarize that the presence of a porous layer always strengthens the slippage at the porous-liquid interface even when the porous layer properties are kept fixed and the viscosity or density ratio or the angle of inclination is increased. Importantly, the slippage at the porous-liquid interface is found to be larger when the lower layer has less density and viscosity. The observations on the base state velocity profiles with various parameters will be of help while discussing the results in the following sections.

IV. LINEAR STABILITY ANALYSIS

Equations (2.16)–(2.37) are linearized using the following linear perturbations to the base state solution: $U_j = \bar{U}_j + U'_j$, $W_j = W'_j$, and $P_j = \overline{P}_j + P'_j$. The primes denote perturbed quantities in which the velocity perturbations are transformed into the stream functions as $U'_j = \partial\Psi_j/\partial Z$ and $W'_j = -\partial\Psi_j/\partial X$. The set of equations are linearized employing normal modes, $\Psi_j(X,Z,T) = \tilde{\Psi}_j(Z)e^{\mathbf{i}K(X-CT)}$, $P'_j(X,Z,T) = \tilde{P}_j(Z)e^{\mathbf{i}K(X-CT)}$, $H_j(X,Z,T) = 1 + \tilde{H}_j e^{\mathbf{i}K(X-CT)}$, to obtain the following coupled OS equations for the films and the porous layer:

$$(D^2 - K^2)^2\tilde{\Psi}_1 = \mathbf{i}K[(\bar{U}_1 - C)(D^2 - K^2) - D^2\bar{U}_1]\tilde{\Psi}_1, \tag{4.1}$$

$$\nu_r(D^2 - K^2)^2\tilde{\Psi}_2 = \mathbf{i}K[(\bar{U}_2 - C)(D^2 - K^2) - D^2\bar{U}_2]\tilde{\Psi}_2, \tag{4.2}$$

$$(D^2 - K^2)^2\tilde{\Psi}_m = (\delta/Da - \mathbf{i}KC)(D^2 - K^2)\tilde{\Psi}_m. \tag{4.3}$$

Here the notation D represents the differentiation with respect to Z ($D \equiv d/dZ$). The notation ν_r is the ratio ($= \mu_r/\rho_r$), K is the wave number, and $C(= C_r + \mathbf{i}C_i)$ is the phase speed. The variables C_r and C_i are the real and imaginary parts of the phase speed, respectively.

The linearized boundary conditions at the porous-solid boundary are

$$\tilde{\Psi}_{mZ}(-D_m) = \tilde{\Psi}_m(-D_m) = 0. \tag{4.4}$$

Here the subscript Z represents the differentiation with respect to Z. The linearized boundary conditions at the porous-liquid interface ($Z = 0$) are

$$\tilde{\Psi}_1 = \tilde{\Psi}_m, \tag{4.5}$$

$$\tilde{\Psi}_{1Z} = \tilde{\Psi}_{mZ}, \tag{4.6}$$

$$\frac{1}{\delta}\tilde{\Psi}_{mZZ} - \tilde{\Psi}_{1ZZ} = \frac{\chi}{\sqrt{\mathrm{Da}}}\tilde{\Psi}_{mZ}, \tag{4.7}$$

$$iK\bar{U}_{1Z}\tilde{\Psi}_1 + [-3K^2 + iK(C - \bar{U}_1)]\tilde{\Psi}_{1Z} + \tilde{\Psi}_{1ZZZ} = \frac{1}{\delta}\left[-3K^2 - \frac{\delta}{\mathrm{Da}} + iKC\right]\tilde{\Psi}_{mZ} + \frac{1}{\delta}\tilde{\Psi}_{mZZZ}. \tag{4.8}$$

The expressions for the linearized boundary conditions at the liquid-liquid interface ($Z = 1$) are given by

$$\tilde{H}_1 = \tilde{\Psi}_1/(C - \bar{U}_1), \tag{4.9}$$

$$\tilde{\Psi}_1 = \tilde{\Psi}_2 \tag{4.10}$$

$$(\tilde{\Psi}_{1Z} - \tilde{\Psi}_{2Z}) + [\tilde{\Psi}_1/(C - \bar{U}_1)](\bar{U}_{1Z} - \bar{U}_{2Z}) = 0, \tag{4.11}$$

$$\tilde{\Psi}_{1ZZZ} - 3K^2\tilde{\Psi}_{1Z} - \mu_r\tilde{\Psi}_{2ZZZ} + 3\mu_r K^2\tilde{\Psi}_{2Z} + iK(C - \bar{U}_1)(\tilde{\Psi}_{1Z} - \rho_r\tilde{\Psi}_{2Z}) + iK(\bar{U}_{1Z}\tilde{\Psi}_1 - \rho_r\bar{U}_{2Z}\tilde{\Psi}_2) - \tilde{\Psi}_1/(C - \bar{U}_1)[(\bar{U}_{1Z} - \mu_r\bar{U}_{2Z})2K^2 + i\Gamma K^3] = 0, \tag{4.12}$$

$$[\tilde{\Psi}_{1ZZ} + K^2\tilde{\Psi}_1] + (\bar{U}_{1ZZ} - \mu_r\bar{U}_{2ZZ})\tilde{\Psi}_1/(C - \bar{U}_1) - \mu_r[\tilde{\Psi}_{2ZZ} + K^2\tilde{\Psi}_2] = 0. \tag{4.13}$$

The linearized boundary conditions at the free surface ($Z = H_2$) are obtained as

$$\tilde{H}_2 = \tilde{\Psi}_2/(C - \bar{U}_2), \tag{4.14}$$

$$3\mu_r K^2\tilde{\Psi}_{2Z} - \mu_r\tilde{\Psi}_{2ZZZ} - iK\rho_r[\bar{U}_{2Z}\tilde{\Psi}_2 + \tilde{\Psi}_{2Z}(C - \bar{U}_2)] + \tilde{\Psi}_2/(C - \bar{U}_2)[ik^3\Gamma_2 + 2\mu_r K^2\bar{U}_{2Z}] = 0, \tag{4.15}$$

$$[\tilde{\Psi}_{2ZZ} + K^2\tilde{\Psi}_2] + (\bar{U}_{2ZZ})\tilde{\Psi}_2/(C - \bar{U}_2) = 0. \tag{4.16}$$

V. NUMERICAL METHOD

The eigenvalue problem in Eqs. (4.1)–(4.16) is solved numerically to obtain the growth rate (KC_i) and wave number (K) for the unstable linear modes. The accurate D^2 algorithm for the Chebyshev-Tau QZ spectral method is employed to obtain the eigenvalues [83–85]. To implement this method the computational domain is mapped into $(-1,1)$ using the transformations $Z_1 = -2Z + 1$, $Z_2 = \frac{2}{H_2-1}Z - \frac{H_2+1}{H_2-1}$, and $Z_m = \frac{2}{D_m}Z + 1$, for the lower, upper, and the porous layers, respectively. Thereafter, the fourth order Ordinary Differential Equation (ODEs) (4.1)–(4.3) are transformed into six second order ODEs in terms of the variables ξ, λ, and ϑ with $\eta(Z_1) = \tilde{\Psi}_1(Z)$, $\sigma(Z_2) = \tilde{\Psi}_2(Z)$, and $\zeta(Z_m) = \tilde{\Psi}_m(Z)$. The equations are obtained as

$$L_1\eta - \xi = 0, \tag{5.1}$$

$$L_1\xi - iK\bar{U}_1\xi + 2iKC_{11}\eta + iKC\xi = 0, \tag{5.2}$$

$$L_2\sigma - \lambda = 0, \tag{5.3}$$

$$\nu_r L_2\lambda - iK\bar{U}_2\lambda + 2iKC_{21}\sigma + iKC\lambda = 0, \tag{5.4}$$

$$L_m\zeta - \vartheta = 0, \tag{5.5}$$

$$L_m\vartheta - \frac{\delta}{\mathrm{Da}}\vartheta + iKC\vartheta = 0. \tag{5.6}$$

Here the operators employed are $L_1\eta \equiv (4d^2/dZ_1^2 - K^2)\eta = \xi$, $L_2\sigma \equiv \{[4/(H_2-1)^2]d^2/dZ_2^2 - K^2\}\sigma = \lambda$, and $L_m\zeta \equiv [(4/D^2)d^2/dZ_m^2 - K^2]\zeta = \vartheta$. The transformed boundary conditions at the porous-solid boundaries in terms of the above variables are

$$\zeta_{Zm}(-1) = \zeta(-1) = 0. \tag{5.7}$$

The transformed boundary conditions at the porous-liquid interface are

$$\eta - \zeta = 0, \tag{5.8}$$

$$\eta_{Z1} + \frac{1}{D}\zeta_{Zm} = 0, \tag{5.9}$$

$$K^2\eta + \xi - \frac{K^2}{\delta}\zeta + \frac{2\chi}{D\sqrt{\mathrm{Da}}}\zeta_{Zm} - \frac{1}{\delta}\vartheta = 0, \tag{5.10}$$

$$iKC_{12}\eta + 2(2K^2 + iK\bar{U}_1)\eta_{Z1} - 2\xi_{Z1} + \frac{2}{\delta D}\left[2K^2 + \frac{\delta}{\mathrm{Da}}\right] \times \zeta_{Zm} - \frac{2}{\delta D}\vartheta_{Zm} - C\left(2iK\eta_{Z1} + \frac{2iK}{\delta D}\zeta_{Z1}\right) = 0. \tag{5.11}$$

The transformed boundary conditions at the liquid-liquid interface are

$$\eta - \sigma = 0, \tag{5.12}$$

$$C[2\eta_{Z1} + (2/H_2 - 1)\sigma_{Z2}] - [(2C_{11} + C_{12}) - (2C_{21} + C_{22})]\eta - 2\bar{U}_1\eta_{Z1} - (2\bar{U}_1/H_2 - 1)\sigma_{Z2} = 0, \tag{5.13}$$

$$C(2K^2\eta + \xi - 2\mu_r K^2\sigma - \mu_r\lambda) + 2[(C_{11} - \mu_r C_{21}) - \bar{U}_1K^2]\eta - \bar{U}_1\xi + 2\mu_r\bar{U}_1K^2\sigma + \mu_r\bar{U}_1\lambda = 0, \tag{5.14}$$

$$\begin{aligned} &C^2[2iK\eta_{Z1} + (2iK\rho_r/H_2 - 1)\sigma_{Z2}] + C[-iK(2C_{11} + C_{12})\eta - 4(iK\bar{U}_1 + K^2)\eta_{Z1} + 2\xi_{Z1} + iK\rho_r(2C_{21} + C_{22})\sigma \\ &- (4/H_2 - 1)(\mu_r K^2 + iK\rho_r\bar{U}_1)\sigma_{Z2} + [2\mu_r/(H_2 - 1)]\lambda_{Z2}], \\ &+ [2[(2C_{11} + C_{12}) - \mu_r(2C_{21} + C_{22})]K^2 + iK\bar{U}_1(2C_{11} + C_{12}) + i\Gamma K^3]\eta + 2(2\bar{U}_1K^2 + iK\bar{U}_1^2)\eta_{Z1} - 2\bar{U}_1\xi_{Z1} \\ &- iK\bar{U}_1\rho_r(2C_{21} + C_{22})\sigma + [2/(H_2 - 1)]\left[2\mu_r\bar{U}_1K^2 + iK\rho_r\bar{U}_1^2\right]\sigma_{Z2} - [2\mu_r\bar{U}_1/(H_2 - 1)]\lambda_{Z2} = 0. \end{aligned} \tag{5.15}$$

The transformed boundary conditions at the liquid-air interface are

$$C(\lambda + 2K^2\sigma) - \bar{U}_2\lambda + 2(\bar{U}_2K^2 - C_{21})\sigma = 0, \tag{5.16}$$

$$\begin{aligned} &C^2[-2iK\rho_r/(H_2 - 1)]\sigma_{Z2} + C\{-iK\rho_r(2BC_{21} + C_{22})\sigma + [(4\mu_r K^2 + 2iK\rho_r\bar{U}_2)2/(H_2 - 1)]\sigma_{Z2} - 2\mu_r/(H_2 - 1)\lambda_{Z2}\} \\ &+ [(iK\rho_r\bar{U}_2 + 2\mu_r K^2)(2H_2C_{21} + C_{22}) + iK^3\Gamma_2]\sigma - \left[\left(iK\rho_r\bar{U}_2^2 + 4\mu_r\bar{U}_2K^2\right)2/(H_2 - 1)\right]\sigma_{Z2} \\ &+ [2\mu_r\bar{U}_2/(H_2 - 1)]\lambda_{Z2} = 0. \end{aligned} \tag{5.17}$$

Here the subscripts $Z1$, $Z2$, and Zm denote ordinary differentiation with respect to these variables. Equations (5.1)–(5.17) are then expanded in terms of Chebyshev polynomials $T_n(z)$. For a Chebyshev polynomial with N terms, the eigenvalues are obtained from a $(6N + 12) \times (6N + 12)$ matrix corresponding to 6 ODEs and 12 boundary conditions. The accuracy of the eigenvalues is ensured by increasing the number of polynomials and then eliminating the spurious eigenvalues. The eigenvalues are verified by solving Eqs. (5.1)–(5.17) employing spectral collocation method with enhanced accuracy [86].

Figure 3(a) shows the typical linear growth rate (KC_i) vs wave number (K) plot for a free bilayer where the eigenvalues are predicted with equal accuracy by both spectral collocation (SC) and Chebyshev-Tau QZ (Tau) algorithms. In Fig. 3(b),

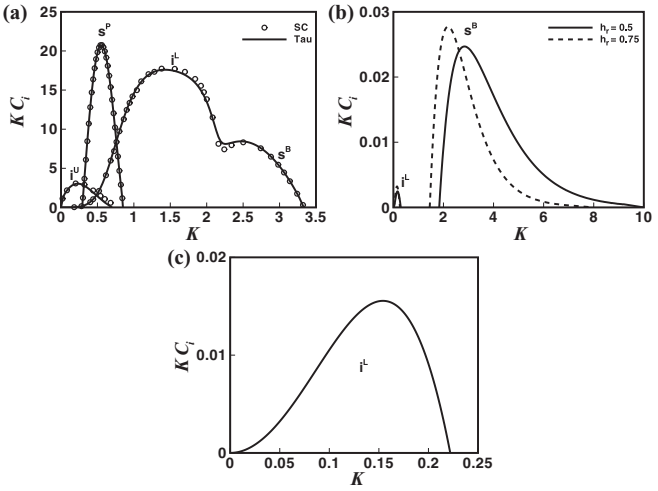

FIG. 3. Plot (a) shows the variation of growth rate (KC_i) with wave number (K). In plot (a) $\delta = 0.5$, $D_m = 1$, Da $= 5 \times 10^{-3}$, $h_r = 1.5$, $\rho_r = 1$, $\mu_r = 0.9$, $\Gamma_1 = 8 \times 10^3$, $\Gamma_2 = 15 \times 10^3$, and $\alpha = 0.2$. The solid line (dots) shows the result from the Chebyshev-Tau QZ (spectral collocation) method. The curve i^{U} represents the surface mode at free surface. i^{L} represents the interfacial mode at liquid-liquid interface, s^{P} represents porous media shear mode, and s^{B} represents shear mode. Plot (b) gives growth rate for different h_r when $\mu_r = 2.5$, $\rho_r = 1$, $\delta = 0.01$, $D_m = 0.01$, Da $= 0.1$, $\Gamma_1 = 0$, $\Gamma_2 = 0$, and $\alpha = 0.2$. For plot (c) $\delta = 0.3$, $D_m = 0.3$, Da $= 0.2$, $h_r = 0.05$, $\rho_r = 1$, $\mu_r = 1$, Re $= 1$, and cot $\alpha = 1$.

we reproduce a pair of linear growth rate (KC_i) vs wave number (K) plot for a free bilayer flowing on a nearly nonslipping and impervious substrate [39] in the limit where the effects of the porous layer is rather trivial. In Fig. 3(c), we asymptotically recover a KC_i vs K plot for single layer flow over porous medium from Ref. [60] under similar conditions. Figure 3 corroborates the accuracy of the codes employed to predict the eigenvalues employed in this study. In what follows, we employ the Chebyshev-Tau QZ algorithm to report the results under varied conditions. The eigenfunctions corresponding to the eigenvalues are obtained employing the spectral collocation method.

VI. RESULTS AND DISCUSSION

Figure 1 schematically shows a thin free bilayer flowing on an inclined porous medium. In the absence of the porous layer, the interfaces in a free bilayer flow over an impervious substrate can be unstable by interfacial modes originating from the viscosity and density stratifications across the liquid-liquid and liquid-air interfaces [36–41]. At higher flow rates, the increasing influence of the inertial forces can also engender finite-wave-number shear modes [17]. In what follows, we discuss the fate of these modes under the influence of porous layer parameters. We also explore the possibility of new unstable modes that are specific to the presence of the porous layer.

The coupled deformable free surface and interface of a bilayer can show interfacial modes of instabilities under the influence of small amplitude perturbation. Depending on the magnitude of the surface (interfacial) tension at the free surface

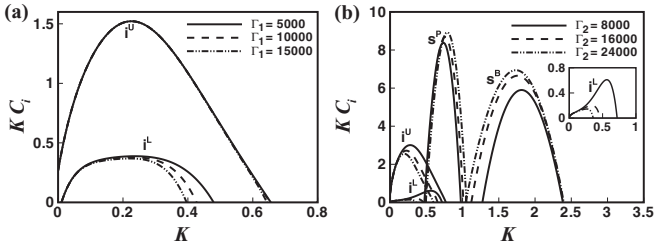

FIG. 4. Plots show the variations of growth rate (KC_i) with wave number (K). The curve i^{U} represents the surface mode at the free surface. i^{L} represents the interfacial mode at the liquid-liquid interface, s^{P} represents porous media shear mode, and s^{B} represents shear mode. The curves in plot (a) correspond to different Γ_1 when Re $= 97$, $\mu_r = 0.5$, and $\Gamma_2 = 15 \times 10^3$. The curves in plot (b) correspond to different values of Γ_2 when Re $= 389$, $\mu_r = 0.9$, and $\Gamma_1 = 8 \times 10^3$. The other parameters are kept fixed at $\delta = 0.5$, $D_m = 1$, Da $= 5 \times 10^{-3}$, $\rho_r = 1$, $h_r = 1$, and $\alpha = 0.2$.

(interface), the wavelengths of these modes can vary. Further, the strongly coupled interfaces can evolve in a single wavelength whereas a weak coupling between the interfaces can engender different wavelengths of interfacial deformations. The growth rate (KC_i) vs wave number (K) plots in Fig. 4 indicate the presence of multiple interfacial modes, i^{L} and i^{U}. Here the superscripts "L" and "U" correspond to the interfacial mode corresponding to "lower" liquid-liquid and "upper" liquid-air interface. The interfacial modes are differentiated based on the phase speed of the unstable interfacial modes corresponding to the base state velocities at the interfaces [38,47]. Plot (a) shows that when the more viscous film is adjacent to the wall, the bilayer is unstable by a dominant i^{U} mode and a subdominant i^{L} mode. Interestingly, the curves in this plot also show that at a fixed Γ_2, an increase in Γ_1 leads to the reduction in the growth rate and increase in the wavelength of the i^{L} interfacial mode whereas the i^{U} mode remains almost insensitive to this change. The plots also suggest that when the surface and the interfacial tensions are nearly identical a stronger coupling between the instability modes is observed as the dominant wavelength of instability becomes similar. Plot (b) also shows that the change in the surface tension has profound influence on both the interfacial modes. However, under this condition the dominant wavelength of instability for the interfacial modes is found to be very different signifying a decoupling of the unstable modes. Figure 4(b) also confirms the presence of a pair of finite wave-number s^{B} and s^{P} shear modes in addition to the interfacial modes in which the surface tension at the free surface is found to have more influence on the s^{B} mode. The superscripts here identify the shear mode for a free bilayer on nonslipping surface (s^{B}) and the porous media mediated shear mode (s^{P}). The origin of the shear modes is discussed in the following section through an eigenfunction analysis.

A free bilayer composed of a pair of immiscible phases such as oil and water can be made unstable on a porous layer when the angle of inclination is progressively increased. In such a situation, we can anticipate the appearance of the different instability modes as the flow inside the configuration becomes stronger as the angle of inclination is increased. Figure 5(a) shows the neutral stability curves in the K_c-Re

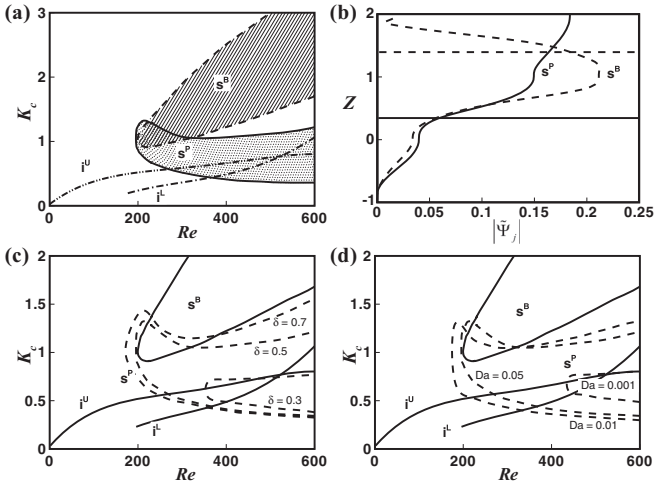

FIG. 5. Plots (a), (c), and (d) show the neutral stability curves. Plot (b) shows the eigenvectors for the s^P and s^B modes at $K = 0.8$ and 1.5, respectively, when $\alpha = 0.16$ (Re = 312). The broken curves in plot (c) show the neutral stability plots with the variation in porosity (δ) and plot (d) shows the same with the variation in Darcy number (Da). The solid lines in the plots (c) and (d) show the other modes. The other parameters chosen for the plots are $\delta = 0.5$, $D_m = 1$, $\mathrm{Da} = 5 \times 10^{-3}$, $\rho_r = 1$, $\mu_r = 0.9$, $h_r = 1$, $\Gamma_1 = 8 \times 10^3$, and $\Gamma_2 = 15 \times 10^3$.

parametric regime for the different instability modes of a free bilayer flowing on a porous medium having constant porosity, permeability, and thickness. In this figure, the area under the curves for the interfacial modes and the shaded area enclosed by the curves for the shear modes show the unstable wave numbers. The curves suggest that the i^U mode can appear even when the configuration is marginally inclined whereas the i^L mode appears only beyond a critical value of Re = 48. The unevenly broken lines confirm the long-wave nature ($KC_i \to 0$ as $K \to 0$) for these interfacial modes, which also shows a larger span of unstable wave numbers at a higher Re. The hashed (shaded) area encompassed by the evenly broken (solid) curve suggests that the finite-wave-number s^P (s^B) shear mode can appear at a larger threshold value of Re (for s^P mode Re = 175; s^B mode Re = 207) when the relatively stronger inertial effects start alleviating the viscous influences. The span of unstable wave numbers for the s^B and s^P shear modes grows with the increase in Re. The s^B mode destabilizes shorter wavelength modes as compared to the other modes. The curves in the Fig. 5(a) reflect that if the flow rate in an oil-water free bilayer is progressively increased the most dangerous is the i^U mode, as it appears at the lowest Re. All the other modes appear at a higher Re and can influence the flow stability in the nonlinear regime, which cannot be unveiled through the present analysis. However, the experiments on the free bilayer flows on a porous medium can also be performed by coating a pair of polymeric films on a porous surface and then heating them well above the glass transition temperature to stimulate flow. In such a situation, the experiments can be initiated with a fixed angle of inclination before the polymer films start moving due to the external heating and i^L, s^B, and s^P modes can be observed at fixed values of Re. Importantly, for a fixed Re the primary mode of instability will be the one growing fastest among all the unstable modes, which we will discuss with Figs. 6–8 in detail.

Figure 5(b) helps in identifying the location of the shear modes through the eigenvectors. While the interfacial modes are always expected to reside in the respective interfaces, the horizontal solid and broken lines show the critical layers corresponding to the s^P and s^B modes, respectively. The solid and broken lines showing the eigenfunctions together with the location of the critical layers confirm the place of the s^B mode in the upper layer and the same of the s^P mode at the lower layer, near the porous-liquid interface. Previous works on the free bilayers flowing over nonslipping and impermeable surfaces report the presence of i^U, i^L, and s^B modes [40,46]. The additional s^P mode at the lower layer originates from the larger flow inside the porous layer. Interestingly, the neutral stability plots in Figs. 5(c) and 5(d) show that increase in the porosity (δ) and permeability (Da) of the porous medium can only influence the s^P mode to originate at a much lower Re while the neutral stability plots for the other modes remain almost invariant. Larger porosity and permeability can allow a stronger flow inside the porous medium even at a smaller inclination (α), which helps the s^P mode to appear at a much lower value of Re. The span of unstable wave number for the s^P mode is also found to increase with Re especially in the shorter wavelength regime. It may be noted here that the interfacial mode appears only beyond a finite inclination and the discontinuity associated with the plot representing the "i^L" mode represents the critical Re at which the mode originates.

Briefly, Figs. 4 and 5 confirm the presence of a pair of interfacial and shear modes for a free bilayer flowing over inclined porous medium in which the interfacial modes are located at the interfaces and the shear s^P and s^B modes are located inside the bulk of the lower and upper layers. The plots suggest that the liquid-air interface is unstable due to the long-wave i^U mode even when the free bilayer is marginally inclined. In contrast, the liquid-liquid interface shows an interfacial mode of instability (i^L mode) at a much larger inclination owing to the lack of viscosity or density stratification across the interface. The shear modes only appear when the flow inside the liquid layers is much stronger and the frictional influences at the layers are progressively reduced by the relatively larger inertial effects. The s^B mode is found to appear at the upper layer near the liquid-air interface because of the weak frictional influence at that location. In comparison, the flow inside the porous layer allows a strong slippage at the porous-liquid interface, which promotes an entirely new s^P mode at the lower layer. It may be noted here that a free bilayer on a nonslipping and impermeable surface never shows the s^P mode because of the stronger frictional influence on the lower layer from the rigid and impermeable wall. In contrast, the presence of the porous layer significantly reduces the frictional influence especially at higher values of porosity, thickness, and permeability, which stimulates the appearance of the s^P mode beyond a critical value of Re.

In Fig. 6 we analyze the coexistence of different instability modes when the parameters related to the films and the porous layers are varied at a finite Re. Plots (a)–(f) show the sensitivities of the linear growth rate (KC_i) with wave number (K) at different δ, D_m, Da, α, h_r, and μ_r, respectively. The

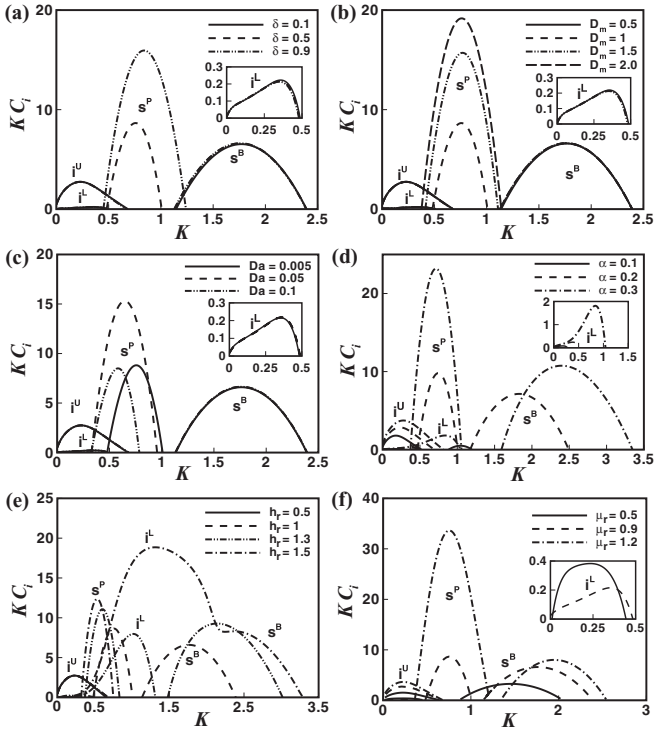

FIG. 6. Plots show the variation of growth rate (KC_i) with wave number (K).The curves in plots (a)–(f) correspond to different δ,D_m, Da, α, h_r, and μ_r, respectively. The other parameters are fixed at $\delta = 0.5$, $D_m = 1$, Da $= 5 \times 10^{-3}$, $\rho_r = 1$, $\mu_r = 0.9$, $h_r = 1$, $\Gamma_1 = 8 \times 10^3$, $\Gamma_2 = 15 \times 103$, and $\alpha = 0.2$.

solid line in plot (a) shows that when the porosity is small the bilayer can be unstable by a pair of long-wave interfacial modes (curve i^{U} and curve i^{L} in the inset) together with a finite-wave-number shear mode (s^{B}). It may be noted here that, in this case, the free surface has larger surface tension as compared to the liquid-liquid interface, which ensures that the i^{L} mode shows a maximum at higher wave number (smaller wavelength) as compared to the i^{U} mode. Interestingly, the i^{U} mode is the dominant one owing to the smaller density and viscosity stratification across the liquid-liquid interface when $\rho_r = 1$, $\mu_r = 0.9$, which leads to a very weak i^{L} mode. The origin of the finite wave-number shear mode s^{B} can be attributed to the increasing inertia inside the bilayer with an increase in the angle of inclination, as discussed in the previous figure. Plot (a) also shows that for a fixed angle of inclination, when the porosity (δ) of the porous layer is progressively increased, a new finite-wave-number s^{P} mode appears (broken curves). In fact, the s^{P} mode can even be the dominant one at higher δ. The origin of this new porous-media s^{P} mode can be attributed to the augmented inertia at the liquid layers owing to the larger slippage at the porous-liquid interface, as previously observed in the base state velocity profiles. The broken lines in plot (b) show that the s^{P} mode also gains strength with the increase in the porous layer thickness (D_m). Interestingly, increase in the permeability of the porous layer (Da) increases the strength of the s^{P} mode until a threshold value as shown by the solid (Da $=$ 0.005) and the evenly broken (Da $=$ 0.05) lines in plot (c). However, beyond this point, a larger flow in the porous layer again decreases the strength of the s^{P} mode, as shown by the evenly (Da $=$ 0.05) and unevenly broken (Da $=$ 0.1) lines in the plot (c). Thus, with the change in permeability the s^{P} mode is found to dominate only for a span of intermediate Da values and remain subdominant or absent otherwise. Plot (d) shows that when the angle of inclination (α) of the substrate increases, all the unstable modes gain strength. This is in contrast to plots (a)–(c) where the porous media parameters could only influence the growth rate corresponding to the s^{P} mode and other instability modes remained rather insensitive to the same influences. Interestingly, plot (d) also shows that although an increase in α increases the strength of all the i^{U}, i^{L}, and s^{B}, it has a more profound impact on the s^{P} mode, as it is observed to be the dominant mode at higher inclinations even at a moderately high porosity ($\delta = 0.5$). Previously, in Fig. 2 it was shown that the slippage at the porous-liquid interface increases with an increase in α, which in turn helps the s^{P} mode to gain dominance over the other modes especially at higher values of α. Plot (e) shows another interesting scenario where the ratio of the upper to lower film thickness (h_r) is varied. When the upper layer is thin (solid line) we observe the presence of a dominant i^{U} mode of instability. With an increase in the upper layer thickness the s^{B} mode progressively gains strength and along with that the i^{L} and the s^{P} modes make an appearance. The growth of the shear modes can be attributed to the reduction in the frictional influence for the bilayers with thicker upper layer. Interestingly, when the upper layer is relatively thicker (dash dot line), we observe the appearance of a bimodal plot, in which the smaller wave-number maximum corresponds to the i^{L} mode and the larger wave-number maximum corresponding to the s^{B} mode. The curves corresponding to $h_r = 1.3$ and 1.5 together confirm that when the unstable wave numbers for the i^{L} and s^{B} modes are very similar, an interference of the unstable wave numbers gives rise to the bimodality of the curves. The unevenly broken lines in plot (f) show that a more viscous upper layer not only destabilizes a free bilayer by simulating the i^{U} and s^{B} modes but also has a significant influence on the s^{P} mode even at a moderately high porosity. In such a situation, the additional inertial influence originating from the porous layer stabilizes the i^{L} mode. In contrast, when $\mu_r < 1$, the i^{L} mode appears and the s^{P} mode disappears. The observation here is again in commensuration to the base state plots in Fig. 2 where we observed a higher (lower) slippage at the porous-liquid interface when the lower layer had smaller (higher) viscosity leading to a larger (smaller) inertial influence. Concisely, Fig. 6 shows that the additional inertial influence inside an inclined porous plane can have a lasting destabilizing influence on the free bilayer, which can indeed be exploited to increase momentum, heat, and mass transfer in the microscale devices.

Plot (a)–(f) in Fig. 7 show the neutral stability plots with the variations in δ, D_m, Da, Γ_r, h_r, and μ_r, respectively. In the neutral stability plots the area under the curves for the interfacial modes and the shaded area enclosed by the curves for the shear modes show the unstable wave numbers. Plots (a)–(c) show that the s^{P} mode appears only beyond a critical value of δ, D_m, and Da. Further, the span of unstable wave numbers for the i^{L}, i^{U}, and s^{B} modes remain undisturbed when δ, D_m, and Da are progressively increased. The range

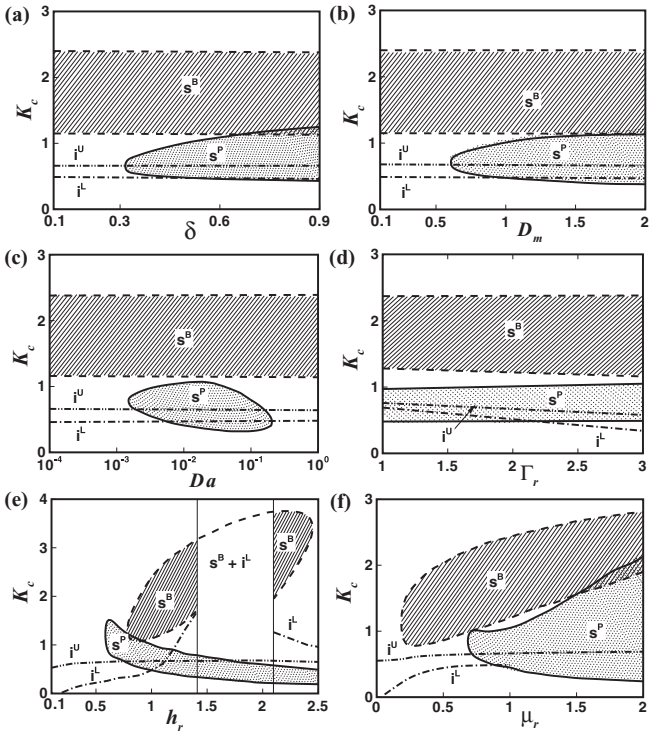

FIG. 7. Plots (a)–(f) show the neutral stability curves with the variations in δ, D_m, Da, $\Gamma_r = \Gamma_2/\Gamma_1$, h_r, and μ_r, respectively. For plot (d) $\Gamma_1 = 8 \times 10^3$ is fixed. The other parameters fixed for the plots are $\delta = 0.5$, $D_m = 1$, Da $= 5 \times 10^{-3}$, $\rho_r = 1$, $\mu_r = 0.9$, $h_r = 1$,$\Gamma_1 = 8 \times 10^3$, $\Gamma_2 = 15 \times 103$, and $\alpha = 0.2$.

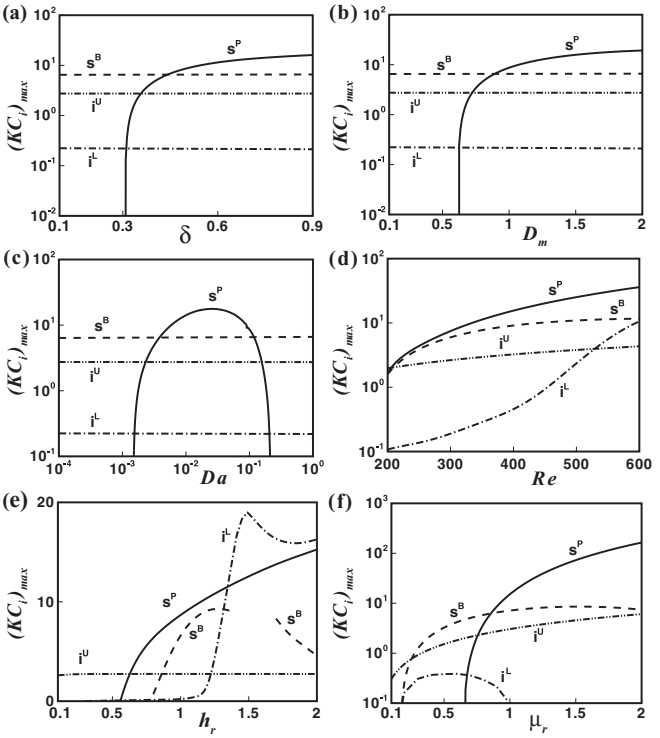

FIG. 8. Plots (a)–(f) show the variation of $(KC_i)_{\max}$ with δ, D_m, Da, Re, h_r, and μ_r, respectively. The other parameters are fixed as $\delta = 0.5$, $D_m = 1$, Da $= 5 \times 10^{-3}$, $\rho_r = 1$, $\mu_r = 0.9$, $h_r = 1$, $\Gamma_1 = 8 \times 10^3$, $\Gamma_2 = 15 \times 10^3$, and $\alpha = 0.2$.

of unstable wave numbers for the s^{P} mode increases with an increase in δ and D_m. The s^{P} mode is stable for small and moderately large range values of Da and is unstable in a closed region in the K_c-Da plane. The plots confirm that when the other parameters are fixed the porous media parameters can only influence the s^{P} mode. In comparison, plots (d)–(f) show that the span of unstable wave numbers for all the modes grows with the increase in Γ_r, h_r, and μ_r, respectively. Plot (d) suggests that the span of unstable wave numbers for the interfacial mode progressively increases with a reduction in Γ_r, whereas the shear modes remain almost insensitive to the change. Interestingly, plot (e) shows the appearance of the i^{L} and s^{B} modes beyond a critical h_r, which gradually merges to a single mode at higher values of h_r (=1.4), as denoted by the "$s^{\mathrm{B}} + i^{\mathrm{L}}$" zone in the area encompassed by the evenly broken line. It may be noted here that in this region, only the bimodal growth rate vs wave-number plots are observed in Fig. 6 At higher values of h_r (=2.1), as the shear mode increasingly shifts more to the smaller wavelength regime due to the excess inertial influence, again the independent identities of the i^{L} and s^{B} modes are recovered. The plots also show that the s^{P} mode makes appearance only beyond a critical h_r (=0.6) as shown by the dotted enclosed region. With an increase in the upper layer thickness, the span of unstable wave numbers for the s^{P} mode shifts towards the longer wavelength regime. Plot (f) shows that both the shear modes appear only beyond a threshold μ_r and a free bilayer with a more viscous upper layer can destabilize a larger span of unstable wave numbers for the s^{P} mode. The plot also shows that the i^{L} mode for a free bilayer flowing over a porous layer exists in the region where $\mu_r < 1$. The s^{B} mode is found to shift towards the shorter wavelength regime as the upper layer becomes more viscous.

In Fig. 8, we find out which of the modes dominate the instability of a free bilayer with the variations in δ, D_m, Da, Re, h_r, and μ_r. The curves in plots (a)–(c) show that at smaller values of δ, D_m, and Da, the instability characteristics are similar to a free bilayer on an inclined impervious surface as the s^{P} mode is absent. Plots (a)–(c) also show that although the i^{L}, i^{U}, and s^{B} modes remain undisturbed (broken lines) when δ, D_m, and Da are progressively increased, the solid lines show that the s^{P} mode (i) progressively becomes the dominant mode with the increase in δ and D_m, and (ii) becomes the dominant mode only for a span of Da, and otherwise remains a subdominant mode. The solid lines in plots (d)–(f) also uncover that even when the porous layer is moderately porous and permeable, the s^{P} mode can be the dominant one at reasonably higher Re, h_r, and μ_r, respectively. The plots also show that a thicker and more viscous upper layer helps in destabilizing the s^{P} mode to a larger extent and all the other modes are found to become subdominant under such conditions. The only exception to this observation is when the i^{L} and s^{B} modes merge and show dominance through bimodality. We interpret the bimodal plots as the i^{L} mode, since the plot loses its finite wave-number characteristics. The discontinuity in the plot (e) for the s^{B} mode is also associated with the same phenomena. Plot (f) suggests that the i^{L} mode is present only when $\mu_r < 1$ for a free bilayer flowing on a porous layer. Concisely, the figure depicts that the addition of a porous layer underneath

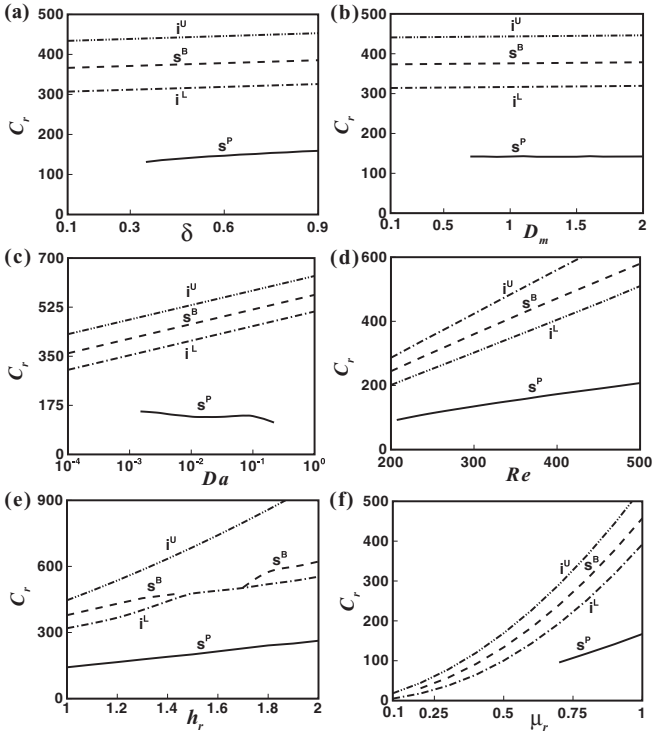

FIG. 9. Plots (a)–(f) show the variation of C_r with δ, D_m, Da, Re, h_r, and μ_r, respectively. The other parameters are fixed as $\delta = 0.5$, $D_m = 1$, Da $= 5 \times 10^{-3}$, $\rho_r = 1$, $\mu_r = 0.9$, $h_r = 1$, $\Gamma_1 = 8 \times 10^3$, $\Gamma_2 = 15 \times 103$, and $\alpha = 0.2$.

a free bilayer can develop a dominant s^{P} mode of instability even for reasonable porosity, thickness, and permeability of the porous layer.

Figure 9 shows the variation in phase speed as a function of dimensionless parameters governing the free bilayer flow on an inclined porous medium. Plots (a)–(c) suggest that phase speed (C_r) is not very sensitive to the porous media parameters except Da whereas plots (d)–(f) show that C_r increases significantly with an increase in Re, h_r, and μ_r. Interestingly, C_r for the s^{P} mode is always found to be smaller than the other modes, which can be explained from its location near the porous-liquid interface, as predicted by the critical layer analysis in Fig. 5(b). The slowly moving s^{P} mode is under the maximum frictional influence because of its proximity to the bounding wall. In comparison, the i^{L} mode at the liquid-liquid interface is found to move faster as it is away from the wall and is under lesser frictional influence. The location of the s^{B} mode at the upper layer helps it to move at a faster speed than the i^{L} mode, while the i^{U} mode moves with highest speed owing to its largest distance from the bounding wall. Interestingly, the C_r plots for the instability modes ($i^{\mathrm{U}} > s^{\mathrm{B}} > i^{\mathrm{L}} > s^{\mathrm{P}}$) follow the same order based on their location from the bounding wall and hence the decreasing frictional influence. It may be noted here that the discontinuities associated with the plots for the s^{P} mode in this figure indicate the parametric domain where it originates or disappears. The mode appears beyond a critical δ, D_m, Re, Da, and μ_r while it disappears beyond a threshold value of Da, as indicated by the plots.

VII. CONCLUSIONS

The instabilities of an inclined free bilayer flowing over a Darcy-Brinkman porous layer have been explored. An Orr-Sommerfeld analysis of the governing equations and boundary conditions is performed to uncover the salient features of the instabilities. The major conclusions are as follows:

(1) A free bilayer can be unstable by a pair of long-wave interfacial modes together with a pair of finite wave-number shear modes originating from the inertial influences at the liquid layers. Like a free bilayer on an inclined impervious surface, all the unstable modes are found to appear beyond a critical flow rate and travel across the space. All the modes are found to gain strength with increase in the angle of inclination, ratios of the upper to lower liquid film thickness, and viscosities. The interfacial mode specific to the liquid-liquid interface (i^{L} mode) is found to be present only under the condition $\mu_r < 1$.

(2) One of the shear modes (s^{P} mode) originates from the augmented inertial influence of the porous layer, which is found to be the dominant mode even at moderate porosity, permeability, and thickness of the porous layer. The strength of the s^{P} mode (a) increases with increase in porosity, (b) initially increases and then remains a constant with increase in porous layer thickness, and (c) initially increases and then reduces with an increase in the permeability of the porous layer. Interestingly, interfacial modes (i^{L} and i^{U} mode) and the conventional shear mode (s^{B} mode) specific to a bilayer on an impervious surface are found to be rather insensitive to the changes in the porous layer parameters.

(3) Although the increase in the ratios of upper to lower film thicknesses and viscosities and the angle of inclination causes larger destabilization to all the modes, by and large, the s^{P} mode dominates over the other modes when the porous medium is moderately porous, permeable, and thick. The additional inertial influence at the porous-liquid interface originating from the flow inside porous media is the major reason behind the growth of the s^{P} mode in a free bilayer flowing down an inclined plane.

(4) An eigenfuction analysis shows that the s^{B} mode originates at the upper layer whereas the s^{P} mode stays at the lower layer, near the porous-liquid interface. Further, the analysis confirms a progressive increase in the phase speed ($i^{\mathrm{U}} > s^{\mathrm{B}} > i^{\mathrm{L}} > s^{\mathrm{P}}$) as the modes are located away from the bounding wall and have lesser frictional influence.

The results reported here highlight the importance of a porous layer underneath a free bilayer flow to expedite interlayer mixing. The reported parameter space for the dominance of the porous media mediated shear mode can be of significance because even a trifling amount of roughness, porosity, and slippage can develop this instability mode in the more realistic situations and improve the efficiency of mixing, separation, heat, and mass transfer especially in the microscale devices.

ACKNOWLEDGMENTS

Support through an initiation grant from IIT Guwahati and of the DST, India through its fast track scheme SR/FTP/ETA-091/2009 are gratefully acknowledged.

APPENDIX

Base state governing equations are

$$\bar{U}_{1ZZ} = -G \sin\alpha, \tag{A1}$$

$$\bar{U}_{2ZZ} = -(1/\nu_r)G \sin\alpha, \tag{A2}$$

$$(1/\delta)\bar{U}_{mZZ} - (1/\mathrm{Da})\bar{U}_m = -G \sin\alpha. \tag{A3}$$

The dimensionless no-slip boundary condition at the porous-solid interface ($Z = -D_m$) is

$$\bar{U}_m = 0. \tag{A4}$$

The dimensionless form of the continuity of velocity, and the stress jump conditions at the liquid-porous interface ($Z = 0$) are

$$\bar{U}_1 = \bar{U}_m, \tag{A5}$$

$$(1/\delta)\bar{U}_{mZ} - \bar{U}_{1Z} - (\chi/\sqrt{\mathrm{Da}})\bar{U}_m = 0. \tag{A6}$$

The dimensionless form of the continuity of velocity and tangential stress balances at the liquid-liquid interface ($Z = 1$) are

$$\bar{U}_1 = \bar{U}_2, \tag{A7}$$

$$\bar{U}_{1Z} = \mu_r(\bar{U}_{2Z}). \tag{A8}$$

The dimensionless stress balance condition at the liquid-air interface ($Z = H_2$) is

$$\bar{U}_{2Z} = 0. \tag{A9}$$

The above governing equations and boundary conditions yield

$$\bar{U}_1 = C_{11}Z^2 + C_{12}Z + C_{13}, \quad 0 \leqslant Z \leqslant 1, \tag{A10}$$

$$\bar{U}_2 = C_{21}Z^2 + C_{22}Z + C_{23}, \quad 1 \leqslant Z \leqslant B, \tag{A11}$$

$$\bar{U}_m = C_{m1}e^{MZ} + C_{m2}e^{-MZ} + C_{m3}, \quad -D_m \leqslant Z \leqslant 0, \tag{A12}$$

$$C_{11} = -G \sin\alpha/2, \tag{A13}$$

$$C_{12} = -2C_{11} - 2\mu_r(H_2 - 1)C_{21}, \tag{A14}$$

$$C_{13} = \left(\frac{\chi(F_+ - F_-) - \sqrt{\mathrm{Da}}(J_+ + J_- - \phi)}{\phi\sqrt{\mathrm{Da}}}\right)C_{m3} - \frac{2(F_+ - F_-)}{\phi}C_{11} - \frac{2\mu_r(H_2 - 1)(F_+ - F_-)}{\phi}C_{21}, \tag{A15}$$

$$C_{21} = -G \sin\alpha/2\nu_r, \tag{A16}$$

$$C_{22} = -2C_{21}H_2, \tag{A17}$$

$$C_{23} = C_{11} + C_{12} + C_{13} + (2H_2 - 1)C_{21}, \tag{A18}$$

$$C_{m1} = \frac{(F_- - 1)C_{m3} - F_-C_{13}}{(F_+ - F_-)}, \tag{A19}$$

$$C_{m2} = -\frac{(F_+ - 1)C_{m3} - F_+C_{13}}{(F_+ - F_-)}, \tag{A20}$$

$$C_{m3} = \mathrm{Da}G \sin\alpha. \tag{A21}$$

Here, $\phi = F_-J_+ + F_+J_-$; $F_+ = e^{\sqrt{\delta/\mathrm{Da}}\,D_m}$; $F_- = e^{-\sqrt{\delta/\mathrm{Da}}\,D_m}$; $J_+ = (\sqrt{1/\delta\,\mathrm{Da}} + \chi/\sqrt{\mathrm{Da}})$; $M = \sqrt{\delta/\mathrm{Da}}$; $J_- = (\sqrt{1/\delta\,\mathrm{Da}} - \chi/\sqrt{\mathrm{Da}})$.

[1] H. S. Yu and E. M. Sparrow, J. Heat Transfer **91**, 51 (1969).
[2] H. H. Hu and D. D. Joseph, J. Fluid Mech. **205**, 359 (1989).
[3] C. D. Han, *Multiphase Flow in Polymer Processing* (Academic, New York, 1981).
[4] P. A. Davidson and R. I. Lindsay, J. Fluid Mech. **362**, 273 (1998).
[5] M. Ehrhardt, J. Fuhrmann, A. Linke, and E. Holzbecher, *Proceedings of FDFC2008—Fundamentals and Developments of Fuel Cell Conference 2008, Nancy, France, 2008*, http://www.wias-berlin.de/publications/wias-publ/run.jsp?template=abstract&type=Preprint&year=2008&number=1375.
[6] P. X. Jiang, M. H. Fan, G. S. Si, and Z. P. Ren, Int. J. Heat Mass Transfer **44**, 1039 (2001).
[7] M. B. Allen, G. A. Behie, and J. A. Trangenstein, *Multiphase Flow in Porous Media. Mechanics, Mathematics, and Numerics* (Springer-Verlag, Berlin, 1988).
[8] A. R. A. Khaled and K. Vafai, Int. J. Heat Mass Transfer **46**, 4989 (2003).
[9] P. G. Drazin and W. H. Reid, *Hydrodynamic Stability* (Cambridge University Press, London, 1981).
[10] P. G. de Gennes, Rev. Mod. Phys. **57**, 827 (1985).
[11] D. D. Joseph and Y. Y. Renardy, *Fundamentals of Two-Fluid Dynamics, Part I, Mathematical Theory and Applications* (Springer-Verlag, New York, 1993).
[12] K. P. Chen, Appl. Mech. Rev. **48**, 763 (1995).
[13] P. A. M. Boomkamp and R. H. M. Miesen, Int. J. Multiphase Flow **22**, 67 (1996).
[14] A. Oron, S. H. Davis, and S. G. Bankoff, Rev. Mod. Phys. **69**, 931 (1997).
[15] R. V. Craster and O. K. Matar, Rev. Mod. Phys. **81**, 1131 (2009).
[16] C.-S. Yih, J. Fluid Mech. **27**, 337 (1967).
[17] A. P. Hooper and W. G. C. Boyd, J. Fluid Mech. **128**, 507 (1983).
[18] D. D. Joseph, M. Renardy, and Y. Renardy, J. Fluid Mech. **141**, 309 (1984).
[19] S. G. Yiantsios and B. G. Higgins, Phys. Fluids **31**, 3225 (1988).
[20] A. P. Hooper and R. Grimshaw, Phys. Fluids **28**, 37 (1985).
[21] A. P. Hooper, Phys. Fluids **28**, 1613 (1985).
[22] A. P. Hooper and W. G. C. Boyd, J. Fluid Mech. **179**, 201 (1987).
[23] A. P. Hooper, Phys. Fluids A **1**, 1133 (1989).
[24] Y. Renardy, Phys. Fluids **28**, 3441 (1985).
[25] Y. Renardy, Phys. Fluids **30**, 1627 (1987).
[26] T. I. Hesla, F. R. Pranckh, and L. Preziosi, Phys. Fluids **29**, 2808 (1986).
[27] F. Charru and J. Fabre, Phys. Fluids **6**, 1223 (1994).
[28] P. Barthelet, F. Charru, and J. Fabre, J. Fluid Mech. **303**, 23 (1995).
[29] F. Charru and P. Barthelet, Physica D **125**, 311 (1999).

[30] F. Albert and F. Charru, Eur. J. Mech. B-Fluids **19**, 229 (2000).
[31] F. Charru and E. J. Hinch, J. Fluid Mech. **414**, 195 (2000).
[32] B. S. Tilley, S. H. Davis, and S. G. Bankoff, J. Fluid Mech. **277**, 55 (1994).
[33] B. S. Tilley, S. H. Davis, and S. G. Bankoff, Phys. Fluids **6**, 3906 (1994).
[34] M. E. Charles and L. U. Lilleleht, J. Fluid Mech. **22**, 217 (1965).
[35] T. W. Kao and C. Park, J. Fluid Mech. **52**, 401 (1972).
[36] T. W. Kao, Phys. Fluids **8**, 812 (1965).
[37] T. W. Kao, Phys. Fluids **8**, 2190 (1965).
[38] T. W. Kao, J. Fluid Mech. **33**, 561 (1968).
[39] D. S. Loewenherz and C. J. Lawrence, Phys. Fluids A **1**, 1686 (1989).
[40] J. Hu, S. Millet, V. Botton, H. Ben Hadid, and D. Henry, Phys. Fluids **18**, 104101 (2006).
[41] K. P. Chen, Phys. Fluids A **5**, 3038 (1993).
[42] W. Y. Jiang, B. Helenbrook, and S. P. Lin, Phys. Fluids **16**, 652 (2004).
[43] M. Amaouche, N. Mehidi, and N. Amatousse, Phys. Fluids **19**, 084106 (2007).
[44] K. Alba, R. E. Khayat, and R. S. Pandher, Phys. Rev. E **77**, 056304 (2008).
[45] P. Gao and X.-Y. Lu, J. Fluid Mech. **608**, 379 (2008).
[46] J. Hu, X. Y. Yin, H. B. Hadid, and D. Henry, Phys. Rev. E **77**, 026302 (2008).
[47] Gaurav and V. Shankar, Phys. Fluids **22**, 094103 (2010).
[48] D. Bandyopadhyay, R. Gulabani, and A. Sharma, Ind. Eng. Chem. Res. **44**, 1259 (2005).
[49] D. Bandyopadhyay and A. Sharma, J. Chem. Phys. **125**, 054711 (2006).
[50] J. S. Jang and S. S. Lee, Sens. Actuators A **80**, 84 (2000).
[51] H. H. Bau, J. H. Zhong, and M. Q. Yi, Sens. Actuators B **79**, 207 (2001).
[52] S. Qian and H. H. Bau, Mech. Res. Commun. **36**, 10 (2009).
[53] O. Ozen, N. Aubry, D. T. Papageorgiou, and P. G. Petropoulos, Phys. Rev. Lett. **96**, 144501 (2006).
[54] D. Bandyopadhyay, P. D. S. Reddy, A. Sharma, S. W. Joo, and S. Z. Qian, Theor. Comput. Fluid Dyn. **26**, 23 (2012).
[55] P. D. S. Reddy, D. Bandyopadhyay, S. W. Joo, A. Sharma, and S. Qian, Phys. Rev. E **83**, 036313 (2011).
[56] B. Ray, P. D. S. Reddy, D. Bandyopadhyay, S. W. Joo, A. Sharma, S. Z. Qian, and G. Biswas, Electrophoresis **32**, 3257 (2011).
[57] B. Ray, P. D. S. Reddy, D. Bandyopadhyay, S. W. Joo, A. Sharma, and S. Qian, Theor. Comput. Fluid Dyn. **26**, 311 (2012).
[58] B. Ray, D. Bandyopadhyay, A. Sharma, S. W. Joo, S. Z. Qian, and G. Biswas, Microfluid. Nanofluid. **15**, 19 (2013).
[59] G. S. Beavers and D. D. Joseph, J. Fluid Mech. **30**, 197 (1967).
[60] J. P. Pascal, J. Phys. D: Appl. Phys. **32**, 417 (1999).
[61] J. P. Pascal, J. Non-Newtonian Fluid Mech. **133**, 109 (2006).
[62] I. M. R. Sadiq and R. Usha, Phys. Fluids **20**, 022105 (2008).
[63] I. M. R. Sadiq and R. Usha, J. Non-Newton. Fluid **165**, 1171 (2010).
[64] A. Samanta, C. Ruyer-Quil, and B. Goyeau, J. Fluid Mech. **684**, 353 (2011).
[65] R. Usha and S. Naire, Chem. Eng. Sci. **89**, 72 (2013).
[66] I. M. R. Sadiq, R. Usha, and S. W. Joo, Chem. Eng. Sci. **65**, 4443 (2010).
[67] J. A. Ochoa-Tapia and S. Whitaker, Int. J. Heat Mass Transfer **38**, 2635 (1995).
[68] U. Thiele, B. Goyeau, and M. G. Velarde, Phys. Fluids **21**, 014103 (2009).
[69] L. E. Payne and B. Straughan, J. Math. Pures Appl. **77**, 317 (1998).
[70] M. H. Chang, F. L. Chen, and B. Straughan, J. Fluid Mech. **564**, 287 (2006).
[71] L. C. Dong and D. Johnson, Int. J. Heat Fluid Flow **26**, 133 (2005).
[72] A. A. Hill and B. Straughan, J. Fluid Mech. **603**, 137 (2008).
[73] A. A. Hill and B. Straughan, Adv. Water Resour. **32**, 1609 (2009).
[74] A. A. Hill and B. Straughan, Proc. R. Soc. London A **465**, 207 (2009).
[75] B. Goyeau, D. Lhuillier, D. Gobin, and M. G. Velarde, Int. J. Heat Mass Transfer **46**, 4071 (2003).
[76] R. Liu, Q. S. Liu, and S. C. Zhao, Phys. Fluids **20**, 104105 (2008).
[77] R. Liu and Q. S. Liu, Phys. Rev. E **80**, 036316 (2009).
[78] R. Liu and Q. S. Liu, Phys. Fluids **22**, 074101 (2010).
[79] Anjalaiah, R. Usha, and S. Millet, Phys. Fluids **25**, 022101 (2013).
[80] A. Samanta, B. Goyeau, and C. Ruyer-Quil, J. Fluid Mech. **716**, 414 (2013).
[81] H. Goyal, A. A. P. Kumar, D. Bandyopadhyay, R. Usha, and T. Banerjee, Chem. Eng. Sci. **97**, 109 (2013).
[82] A. A. P. Kumar, H. Goyal, T. Banerjee, and D. Bandyopadhyay, Phys. Rev. E **87**, 063003 (2013).
[83] J. J. Dongarra, B. Straughan, and D. W. Walker, App. Numer. Math. **22**, 399 (1996).
[84] S. A. Orszag, J. Fluid Mech. **50**, 689 (1971).
[85] D. Gottlieb and S. A. Orszag, *Numerical Analysis of Spectral Methods: Theory and Applications* (Capital City Press, Montpelier, Vermont, USA, 1993), Sixth printing.
[86] J. A. C. Weideman and S. C. Reddy, ACM Trans. Math. Soft. **26**, 465 (2000).